Physics of Fluids ARTICLE scitation.org/journal/phf

Investigation of the three-dimensional flow past a flatback wind turbine airfoil at high angles of attack

Cite as: Phys. Fluids **33**, 085106 (2021); doi: 10.1063/5.0055822
Submitted: 3 May 2021 · Accepted: 9 July 2021 ·
Published Online: 3 August 2021

Marinos Manolesos[1,a] and George Papadakis[2,b]

AFFILIATIONS

[1]Faculty of Science and Engineering, Swansea University Bay Campus, Fabian Way, SA1 8EN Swansea, United Kingdom
[2]School of Naval Architecture and Marine Engineering, National Technical University of Athens, Zografou Campus, 9 Iroon Polytechniou str, 15780 Athens, Greece

[a)]**Author to whom correspondence should be addressed**: marinos.manolesos@swansea.ac.uk
[b)]papis@fluid.mech.ntua.gr

ABSTRACT

Flatback airfoils are airfoils with a blunt trailing edge. They are currently commonly used in the inboard part of large wind turbine blades, as they offer a number of aerodynamic, structural, and aeroelastic benefits. However, the flow past them at high angles of attack (AoA) has received relatively little attention until now. This is important because they usually operate at high AoA at the inboard part of Wind Turbine blades. The present investigation uses Reynolds averaged Navier–Stokes (RANS) and hybrid RANS + large eddy simulation predictions to analyze the flow in question. The numerical results are validated against previously published wind tunnel experiments. The analysis reveals that to successfully simulate this flow, the spanwise extent of the computational domain is crucial, more so than the selection of the modeling approach. Additionally, a low-drag regime observed at angles of attack before stall is identified and analyzed in detail. Finally, the complex interaction between the three-dimensional separated flow beyond maximum lift (stall cells) with the vortex shedding from the blunt trailing edge is revealed.

INTRODUCTION

As wind turbines grow in size in order to reduce the levelized cost of energy (LCOE), their blades become more slender and more flexible, posing a significant challenge for designers: How can we increase aerodynamic performance and improve blade aeroelastic behavior with limited chord length?

One of the answers to this technical issue is the use of flatback (FB) airfoils at the inboard part of the blades.[1,2] FB airfoils are airfoils with finite trailing edge (TE) thickness. They provide a number of advantages compared to thin TE airfoils of the same thickness. They have improved performance in terms of maximum lift and also provide reduced surface roughness sensitivity,[3] which is crucial for wind turbines. The use of FB airfoils in blades also increases blade flapwise stiffness and reduces blade weight significantly.[1] From a structural point of view, FB profiles offer more space for blade spars to go through, as they have larger cross-sectional area. Unsurprisingly, these benefits come at the cost of increased drag, caused by the low pressure at the blunt TE. To reduce the drag, a number of TE flow control devices have been proposed in the past.[4–6]

Given these characteristics, most of the FB airfoil profile studies to date have focused either on the aerodynamic/aeroacoustic performance of the profiles[6–9] or on the wake characteristics of the flow,[10–14] almost entirely at $\alpha = 0°$ or low angles of attack (AoA). On the contrary, the separated flow over FB profiles has received limited attention up until now. According to Ref. 5, the separated flow past thick FB airfoils is three-dimensional (3D) and coherent structures known as stall cells form. Stall cells are large-scale 3D structures of separated flow that consist of two counter-rotating vortices[15–19] that form on the suction side of airfoils experiencing TE stall.[20]

Additionally, the literature suggests that in high Re number experiments and simulations,[13,21–24] reduced drag values are observed just before stall. This phenomenon has also received practically no research interest. In fact, while the wake structure downstream of cylinders has received significant attention, this is not the case for the wake of streamlined bodies[25] and even less so for FB airfoils at high Reynolds numbers.[26] However, secondary instabilities in the wake of bluff bodies can be used to implement efficient flow control strategies[27–30] and their knowledge is crucial. These are knowledge gaps that

need to be covered, since FB profiles are now commonly used in wind turbine design. An improved understanding of their characteristics is necessary to gain the greatest benefits from their use.

The combination of the three-dimensional unsteady bluff body wake from the blunt TE with the three-dimensional unsteady Stall Cell (SC) flow makes the numerical investigation of this flow a challenge for computational fluid dynamics (CFD). More traditional methods like Reynolds averaged Navier–Stokes (RANS) solvers can provide only reasonable force predictions for FB airfoils and they tend to non-physically damp the flow.[31] If wake characteristics are of interest, then higher fidelity approaches like detached eddy simulations (DES), are more suitable.[10,11,32]

In general, mesh resolution and the size of the domain are crucial factors.[8,33–35] Until now most investigations at high Reynolds numbers concern low aspect ratio (AR) studies,[8,33–39] although it is generally agreed that high AR simulations are required if the wake characteristics are to be captured. SC simulations also need to be of sufficiently high AR,[17,18,40–42] if the phenomenon needs to be captured.

The present study, a continuation of the work presented in Refs. 10, 11, and 32, has a dual aim. On one hand, to identify a suitable numerical approach for the study of the complex flow in question and on the other, to use the validated high-fidelity simulations to analyze the flow and its characteristics. More specifically, we investigate the significance of the flow modeling approach and the spanwise length of the computational domain. Additionally, we intend to identify the low-drag regime at angles of attack just before stall and to investigate the complex wake at AoA beyond stall.

This report continuous with a description of the "Methodology" section, followed by the "Results" section. In the latter, first the effect of the computational domain width is investigated and then the flow past a FB airfoil at high AoA is examined in detail. The paper closes with the "Discussion and Conclusions" section.

METHODOLOGY

Numerical framework

The computational tool used throughout the paper is MaPFlow. MaPFlow is an unsteady (URANS) solver developed at the National Technical University of Athens.[12] It is a cell centered CFD Solver that can use both structured and unstructured grids. It is capable of solving compressible flows, as well as fully incompressible flows using the artificial compressibility method.[43] Additionally, incompressible flows with small compressibility effects are feasible using low-Mach preconditioning. In all cases, the convective fluxes are discretized using the approximate Riemann solver of Roe.[44] For the reconstruction of the flow field, a second-order piecewise linear interpolation scheme is used.[12] The viscous fluxes are discretized using a central second-order scheme. The Venkatakrishnan limiter[45] is utilized when need (in cases of shock waves) nevertheless; in this work, no limiting is employed, since the flow is nearly incompressible, and erroneous activation of flux limiting in the smooth region of the flow can degrade the overall accuracy. Finally, the Green–Gauss approach is used to evaluate gradients of the flow at cell centers.

MaPFlow can handle both steady and unsteady flows. Time integration is achieved in an implicit manner permitting large Courant–Friedrichs–Lewy (CFL) numbers. The unsteady calculations use a second-order time accurate scheme combined with the dual time-stepping technique to facilitate convergence.[46]

MaPFlow is parallelized using the MPI library in a multiblock fashion in which each processor solves a partition of the original computational domain. MaPFlow's parallel performance has been investigated in High Performance Computing (HPC) platforms where the scalability of the code up to thousands of processors is verified.

Turbulence closures implemented on MaPFlow include the one equation turbulence model of Spalart–Allmaras (SA)[47] as well as the two-equation turbulence model of Menter [k–ω Shear Stress Transport (SST)].[48] Regarding higher fidelity models improved delayed DES (IDDES) as defined in Ref. 49 is employed. In the present study, limited 2D and 3D unsteady RANS with the SA turbulence model are reported and the main focus is on 3D simulations with the IDDES. RANS remain the industry standard when it comes to CFD simulations and are hence included in this investigation. The computational cost of wall resolved large eddy simulation remains prohibitive at this Reynolds number and aspect ratio, hence the use of IDDES was selected as a compromise.

Computational grids

In the present study, 3D simulations using the unsteady RANS approach with the SA turbulence model and the IDDES variant are performed. For IDDES simulations, the generation of a suitable computational grid is critical. On the one hand, in the near-wall region, the grid must be coarse enough to ensure that it will be handled by the RANS part of the model while in the wake the grid must be refined accordingly. Following the authors' previous studies[10,11] in this work, a 12×10^6 cell grid is generated.

In the near airfoil region, a grid consisting of hexahedral cells is generated, while in the rest of the domain, an unstructured grid composed of tetrahedral cells is employed. The hexahedral structured-like region extends 0.1 chords around the airfoil and consists of 100 points in the normal-to-the-wall direction while the airfoil is discretized using 430 nodes.

In this region, the y+ value is approximately 0.1 which makes the near wall region appropriate for RANS simulations. In order to achieve these y+ values the first cell center is located 1×10^{-6} non-dimensional units from the wall while in the spanwise and chordwise direction the cell is two orders of magnitude bigger. This type of spacing ensures that the IDDES model in the boundary layer (BL) region is switched off. More specifically, the switch from RANS to DDES brand is accomplished by altering the distance from the wall used in the original model according to

$$l_{DDES} = l_{RANS} - f_d max(0, l_{RANS} - l_{LES}),$$

where l_{RANS} is the distance from the wall (original SA model) and $l_{LES} = C_{DES}\Psi\Delta$ where C_{DES} is an empirical constant and Ψ a low Reynolds number correction. The local length scale Δ is defined as

$$\Delta = min[max(C_w d_w, C_w h_{max}, h_{wn}), h_{max}],$$

where C_w is an empirical constant, d_w is the distance for the wall, h_{wn} is the mesh step in the wall normal direction, and $h_{max} = max(\Delta x, \Delta y, \Delta z)$. Since the mesh is constructed in the BL region to have a large AR $l_{DDES} = l_{RANS}$ is ensured.

In the spanwise direction, a constant spacing was of $\Delta z = 0.008$ (125 spanwise locations) is used, based on the findings of Ref. 11. In the wake region and up to five chords downstream, an unstructured grid is composed of tetrahedral cells. Beyond that point and toward

TABLE I. Selected flow metrics.

		0° experiment[5]	0° IDDES	12° IDDES
Vortex formation length	L_f	$0.75h_{TE}$	$0.75h_{TE}$	$1.15h_{TE}$
Wavelength of primary instability	λ_x	No data available	$3.6h_{TE}$	$3.3h_{TE}$
Wavelength of secondary instability	λ_z	No data available	$1.0h_{TE}$	$1.4h_{TE}$

the computational boundary, the grid gradually coarsens. Regarding the spanwise size of the wing used in the numerical simulations four different AR, namely, 0.2, 0.5, 1, and 2. All the computational grids are identical 2D-wise, while only the length of the wing in the spanwise direction varies.

Symmetry conditions were applied at the side boundaries of the computational domain. It is noted here that a rational choice would be that of periodic lateral boundaries; nevertheless, the numerical results are compared with measurements of a finite AR wing, and therefore, symmetry conditions at the sides were preferred. It is noted that it was not attempted to simulate the wind tunnel sidewall boundary layer as no data were available regarding its characteristics. This is a no trivial task,[50] out of the scope of the present investigation. Overall, the symmetry conditions were selected as a suitable compromise.

Regarding the far-field boundary, it was located 100 chords away from the wing to minimize the influence of the external boundary conditions on the simulations.[51] All the simulations consider the flow fully turbulent. Finally, due to the thick TE, the flow was considered unsteady in all cases.

Validation

The present work builds on previous studies,[10,11] where the numerical framework was validated. A comparison between experimental stereo particle image velocimetry (PIV), hot-wire anemometry, and pressure data at $\alpha = 0°$ can be found in Ref. 10, while the grid dependence of results is discussed in Ref. 11. The numerical predictions for the dominant St number are close to the experimental results, but lower, in agreement with Ref. 8. As discussed in Ref. 10, an increase in the mesh size from 12 (which is the mesh size of the present investigation) to 25 M does not alter the dominant St number.

In the present case, the comparison is extended to force coefficients at higher angles of attack (Fig. 6), surface flow visualization, and wake characteristics (vortex formation length) at $\alpha = 0°$ (Table I). The discrepancies observed at angles of attack beyond maximum lift are linked with stall cell formation and their tendency to provide bifurcating flows in either experiments[41] or simulations.[52] The interested reader is directed to Refs. 10 and 11 and the comparisons are not repeated here in the interest of brevity.

Measurements

The CFD simulations are compared the wind tunnel data from Ref. 5. The experiments concerned a 30% thick FB airfoil with a 10.6% thick TE (LI30-FB10). The airfoil is designed by adding thickness to the mean camber line of a low-induction rotor profile.[53] In the experiments, the wing model had a chord of $c = 0.5$ m and an aspect ratio of $AR = 2.0$, while the chord Reynolds number was 1.5×10^6. The lift was integrated from pressure tap measurements around the airfoil chord at midspan, while drag was measured with a wake rake for attached flow conditions and it was assumed equal to pressure drag for cases with the separated flow. Stereo PIV and hot wire anemometry measurements were taken in the locations shown in Fig. 1. The 95% confidence interval for the lift and drag values is 1% and 4%, respectively. All measurements refer to free transition cases, but it is noted that fixing transition had minimal effect on the performance of the specific profile.[53] Extensive details on the wind tunnel test setup can be found in Ref. 5.

RESULTS

AR study: How much is enough?

In this section, the results from simulations with different AR are examined, from $AR = 0.2$ to $AR = 2.0$. Two different 3D phenomena are involved in the flow in question. On one hand, there is the 3D bluff body shedding downstream of the blunt TE that begins at prestall AoA and on the other hand, we have the 3D stall cells that develop poststall. It is vital to assess what the minimum suitable computational domain is to study this flow. Both IDDES and URANS data are reported in this section.

Bluff body shedding

Figure 2 shows the mean lift and drag coefficient values at $\alpha = 0°$ for the different AR values. Results show that while the lift mean value remains largely unaffected, the standard deviation is reduced with AR increase. The drag mean value and standard deviation are reduced as AR increases, too, and the results approach the experimental value. Going from $AR = 1$ to $AR = 2$ does not alter either the mean values or the standard deviation of either lift or drag.

For completeness, URANS results are also given in this plot, where the $AR = 0$ data correspond to the 2D simulations. The latter significantly overpredict drag value and standard deviation, but lift and drag predictions are closer to IDDES values for AR = 1.0, in agreement with Ref. 10. These observations suggest that the inherent 3D character of the bluff body flow is artificially constrained for the low AR cases ($AR < 1$).

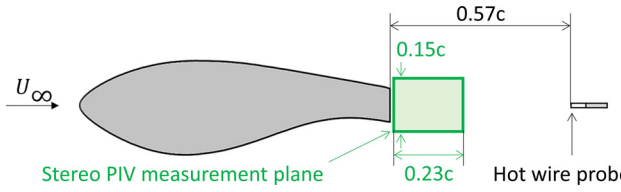

FIG. 1. All cases concern a 30% thick FB airfoil with a 10.6% thick TE (LI30-FB10 from Ref. 53). The schematic shows the experimental setup with the location of the hot wire probe in the wake and size of the stereo PIV measurement plane.

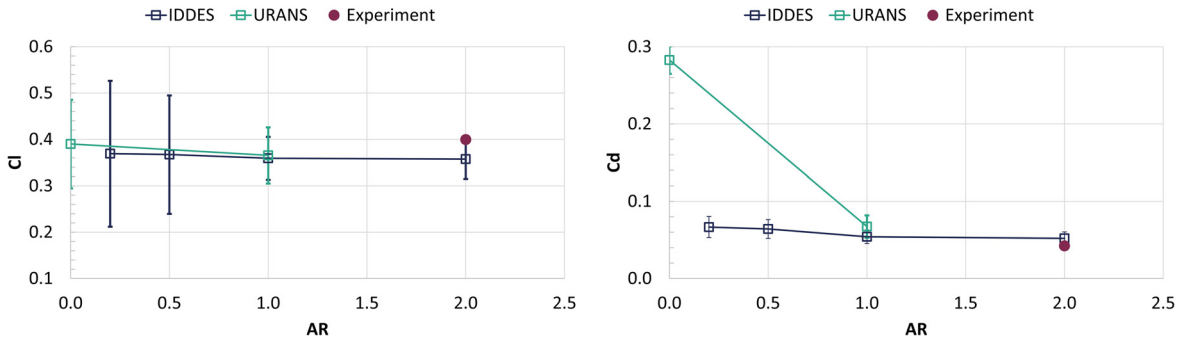

FIG. 2. Force coefficient variation with *AR* for IDDES and RANS simulations of different aspect ratio values at $\alpha = 0°$ and $\mathrm{Re} = 1.5 \times 10^6$. The error bars show standard deviation of the relative quantity and the experimentally measured value is plotted as a dashed line. $AR = 0$ correspond to the 2D case. The inset figure on the right is a close-up at the low drag values.

The spectral content of the drag coefficient time series is given in, Fig. 3 left. The Strouhal number for this case is based on the TE height ($St = \frac{fh_{TE}}{U_\infty}$). The spectra from all cases are very similar, all having a dominant frequency of St $\approx$ 0.21, which corresponds to bluff body shedding. This indicates that even the lowest AR simulations are able to capture the dominant phenomenon (von Kármán–Bénard vortex street). A second peak is observed at the second harmonic, which is because drag is affected similarly by both vortices shed from the TE. The lift coefficient spectrum (not shown here for brevity) provides only the main frequency peak. Interestingly, the peak amplitude at the dominant frequency is reduced as AR increases up to $AR = 1.0$. With increasing AR, the 3D disturbances allow for the redistribution of the energy content of the spectrum among the "near-peak" frequencies. Again, it appears that for $AR > 1.0$, there is no significant difference. In agreement with the previous observation, that low AR simulations artificially constrain the 3D character of the flow, it appears that the lower the AR the more dominant the 2D von Kármán–Bénard shedding appears to be in the flow.

In order to identify the spanwise correlation length in the flow, the Pearson correlation coefficient (r) of the pressure signal at different spanwise locations is presented in Fig. 4. The correlation coefficient is calculated with respect to the pressure at a point located on the TE, at midheight and at midspan [i.e., at $(x/c, y/c, z/b) = (1, 0, 0)$]. The flow appears strongly correlated in the spanwise direction for the low AR cases ($r \approx 1$ for $AR = 0.2$ and 0.5). On the contrary, for $AR \geq 1.0$, the maximum spanwise correlation length appears to be $\lambda \approx 0.3c$, where c is the chord length. In agreement with previous observations, this suggests that the 3D character of the flow requires a wide enough computational domain ($AR > 0.5$) to fully develop.

These correlation lengths are linked to the behavior of the von Kármán–Bénard vortices shed from the airfoil's blunt TE. In practice, these spanwise vortices experience oblique shedding, vortex dislocations and breakdown. Looking at the concentrated vortices (visualized by isosurfaces of the Q criterion[54,55]) in Fig. 5, it appears that for such phenomena to be modeled in a CFD simulation the AR needs to be greater than at least 0.5, or if expressed in terms of the TE height (h_{TE}), the computational domain width should be greater than $\sim 5h_{TE}$.

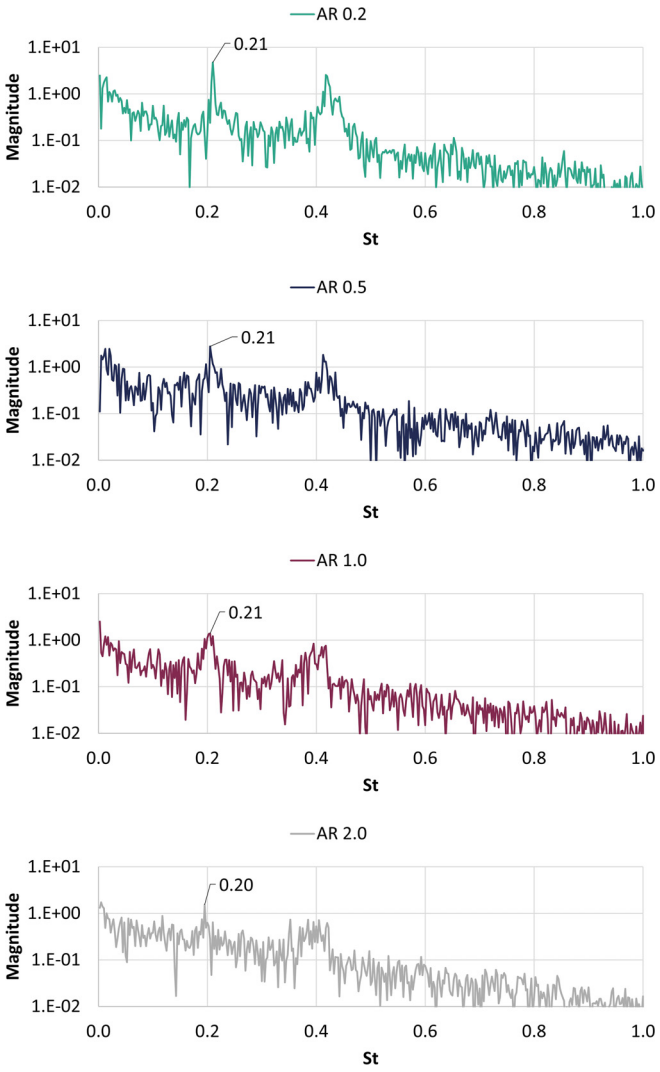

FIG. 3. Frequency spectrum based on the drag coefficient time series for IDDES simulations of different aspect ratio values at $\alpha = 0°$ and $\mathrm{Re} = 1.5 \times 10^6$. The last 20 000 steps of the simulations were used to exclude transient effects.

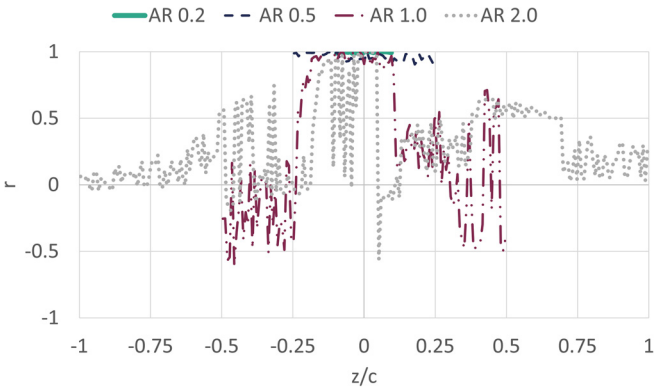

FIG. 4. Pearson correlation coefficient (r) of the pressure time series at the trailing edge midheight with respect to the midsection (placed at z/b = 0) for IDDES simulations of different aspect ratio values at $\alpha = 0°$ and $Re = 1.5 \times 10^6$. Highly positive values indicate a strong positive correlation, and highly negative values suggest a strong negative correlation.

Stall cell formation

Moving to even higher AoA, we see in Fig. 6, left, that $\alpha_{C_l,\max}$ depends on the computational domain *AR*: the higher the *AR* the lower the predicted $\alpha_{C_l,\max}$ is. For $AR \geq 1.0$ maximum lift appears at $\alpha_{C_l,\max} = 13°$, practically equal to the experimental value of $\alpha_{C_l,\max} = 12.6°$. For lower *AR* values $\alpha_{C_l,\max}$ is overpredicted by 2°.

The reason for this discrepancy is that low AR simulations do not allow for SC formation. As indicated in Refs. 15, 17, and 41, for the case of extruded airfoils, *AR* values of $AR \geq 1.0$ are required for SC structures to form. Indeed, the time-averaged surface streamlines shown in Fig. 7 reveal the 3D structure of the flow on the airfoil suction surface for the $AR \geq 1.0$ cases, at $\alpha = 15°$. It is also observed that the three-dimensionality of the flow on the wing surface significantly affects the flow in the wake as well. The separation line vortex and the trailing edge vortex are three-dimensional, growing at the center of the SC, as originally described in Ref. 17.

It is noted that for $AR = 1.0$ only half a SC is formed, while for $AR = 2.0$, two half cells are formed, or the equivalent of a single full SC. The number of stall cells depends on the tip condition and AoA.[56] Present results are in agreement with the experimental investigations from Ref. 5, where a single SC was observed at 15° using oil flow visualization on the AR 2.0 wing model, see Fig. 8. It is noted that SC flow is notorious for providing bifurcating flows[41,57,58] and multiple numerical solutions[41,52] under the same conditions. The fact that two half stall cells are formed in the AR = 2.0 simulations instead of a single SC, as in the experiment, is attributed to the different end wall conditions between and the simulation and experiment. Besides, according to Ref. 52, different solutions might occur due to minor differences in the implementation of boundary conditions, in initial conditions, grid resolution, etc.

The instantaneous flow past the airfoil for different *AR* values at $\alpha = 14°$ and $\alpha = 15°$ is shown in Figs. 9 and 10, respectively. In both cases, there is no SC formation in the low AR simulations. Stall cells

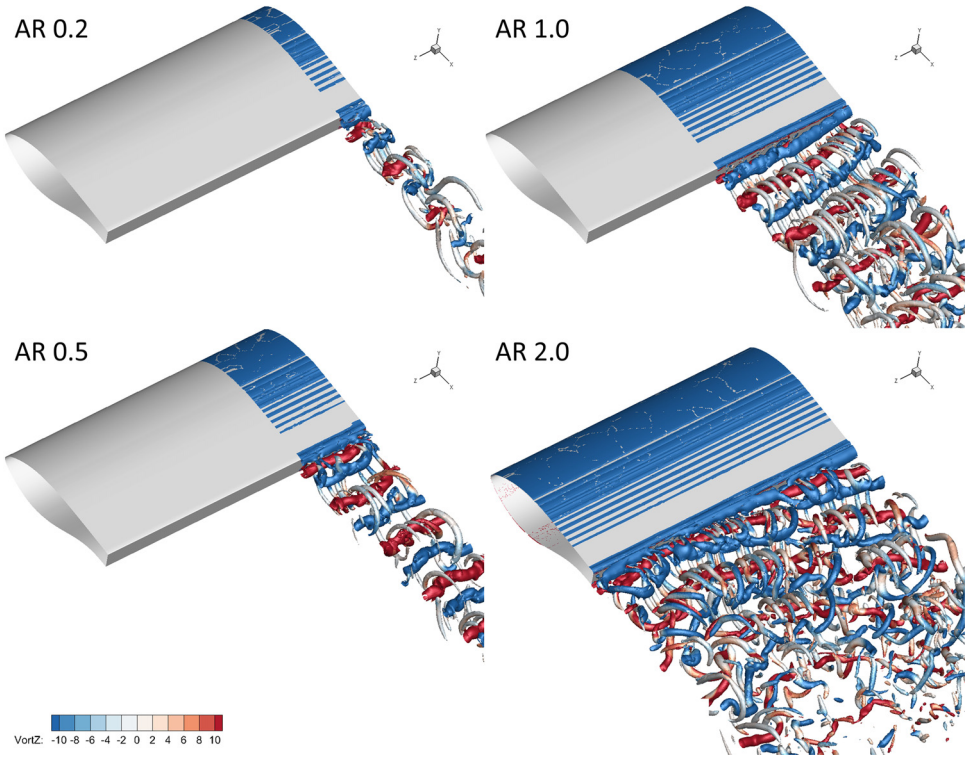

FIG. 5. Q criterion instantaneous isosurfaces of Q = 100 colored by spanwise vorticity. IDDES simulations of different aspect ratio values at $\alpha = 0°$ and $Re = 1.5 \times 10^6$.

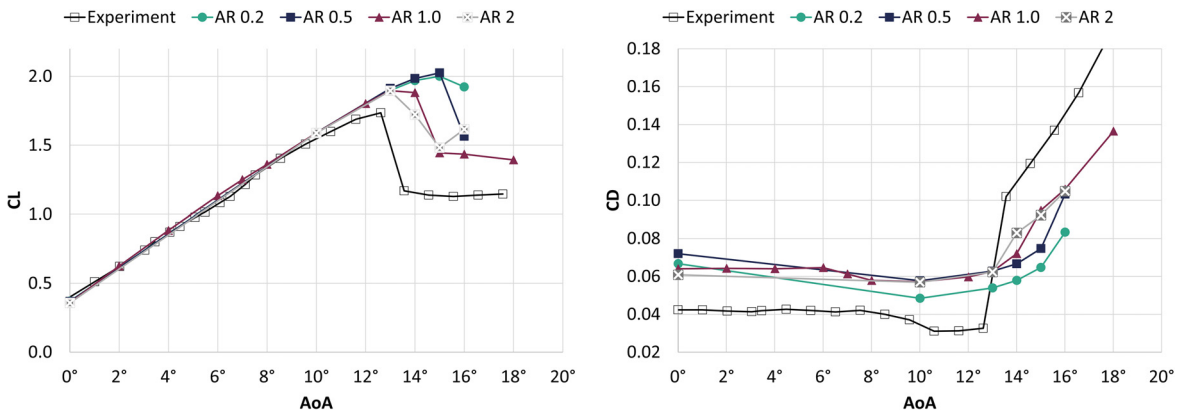

FIG. 6. Lift and drag coefficient variation with angle of attack for IDDES simulations of different aspect ratio values and Re = 1.5×10^6. The experimental data are from Ref. 5.

form initially at $\alpha = 14°$ for $AR = 2.0$ and at $\alpha = 15°$ for $AR = 1.0$. It is worth noting that the SC that forms at $\alpha = 14°$ for $AR = 2.0$ has a larger spanwise width than the stall cells at 15°, where the SC width is equal to 2c. In this respect, there is very good agreement between experiments, $AR = 1.0$ and $AR = 2.0$ simulations.

Flow analysis

In this section the flow in question is examined in detail in terms of force coefficient mean values and time correlations, as well as frequency domain characteristics and spanwise correlations. Finally, the wake structure is examined in detail. Based on the findings of "Stall

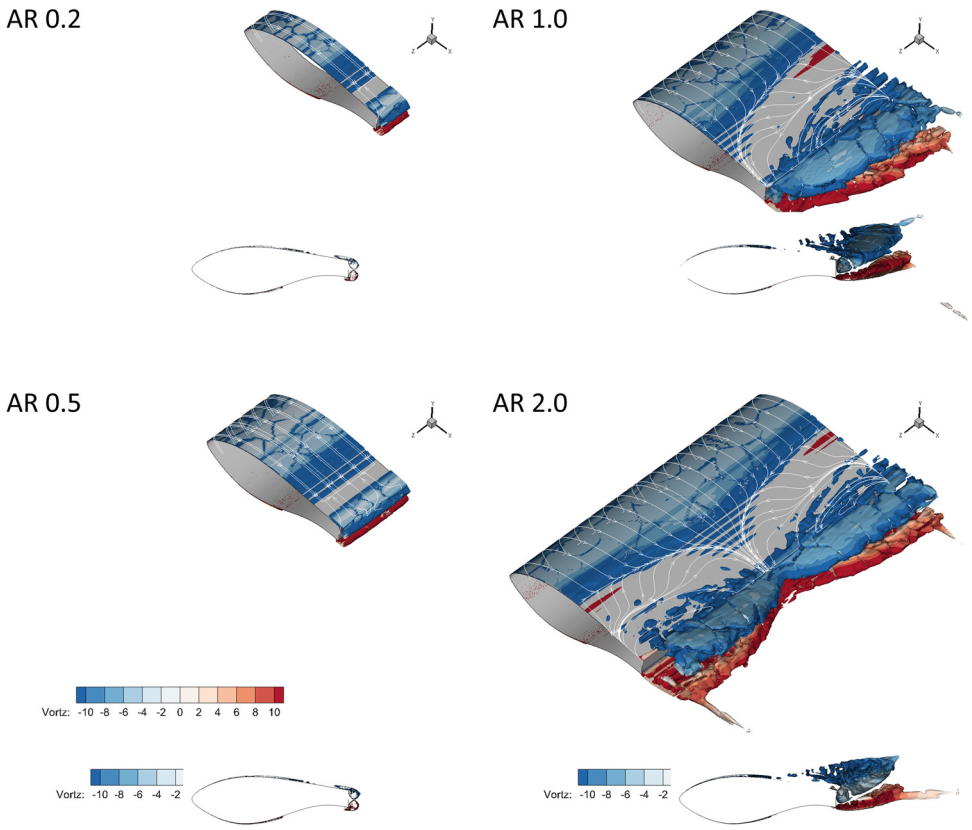

FIG. 7. Time-averaged isosurfaces of Q criterion (Q = 3) colored by spanwise vorticity (VortZ). Surface streamlines are shown on the wing surfaces. IDDES simulations of different aspect ratio values at $\alpha = 15°$ and Re = 1.5×10^6. 3D view and inset side-view are shown for each case.

FIG. 8. Flow visualization on the airfoil suction side, $\alpha = 15°$, $Re = 1.5 \times 10^6$. The flow is from top to bottom and gravity is from right to left, as the model was located vertically in the wind tunnel. Thin white lines highlight the wing leading edge and trailing edge. Reflection from the UV light used to take the photograph is visible close to the LE. Tapes were used to cover the pressure taps during the flow visualization tests. Modified from Ref. 5.

cell formation" section, the IDDES simulations with AR = 1.0 are used for this analysis as they provide the required width for the flow mechanism to develop. URANS simulations of the same AR are also discussed, but only the mean force values are examined for comparisons. It has been shown[10] that URANS simulations artificially damp this type of flow and so statistics or frequency domain characteristics are not examined. For the remaining of the text, IDDES and URANS simulations will refer to the corresponding AR = 1.0 simulations, unless otherwise stated.

Force coefficients

Time domain. The lift and drag polars for the two different modeling approaches are shown in Fig. 11. It is observed that the agreement at low AoA ($0° \leq \alpha \leq 6°$) is good. Then, at $\alpha = 7°$ the lift gradient for the IDDES simulation drops slightly until $\alpha = 13°$. The lift standard deviation in this AoA range, as shown in Fig. 12, left, is smaller than in the low AoA range. Then at $\alpha = 14°$ ($\alpha_{C_l,\max}|_{IDDES}$) the lift coefficient increases slightly, while its variation increases significantly.

For the URANS simulation, the lift gradient remains constant up to $\alpha = 10°$, while it is reduced to a lower constant value in the range $11° \leq \alpha \leq 14°$. At $\alpha = 14°$ ($\alpha_{C_l,\max}|_{RANS}$) the maximum lift value is observed, as in the IDDES simulations. In the reduced lift gradient range ($11° \leq \alpha \leq 14°$), the lift standard deviation is reduced, as the error bars indicate and again as is in the IDDES simulations. The post-stall lift level is higher in the URANS predictions compared to the IDDES results.

Looking at the drag variation with AoA (Fig. 11, right), it is observed that there is a low-drag pocket for both modeling approaches, albeit at different incidence ranges (IDDES: $7° \leq \alpha \leq 13°$, URANS: $11° \leq \alpha \leq 14°$). In that range, the drag coefficient variation is also reduced, as shown in Fig. 12, left for the IDDES

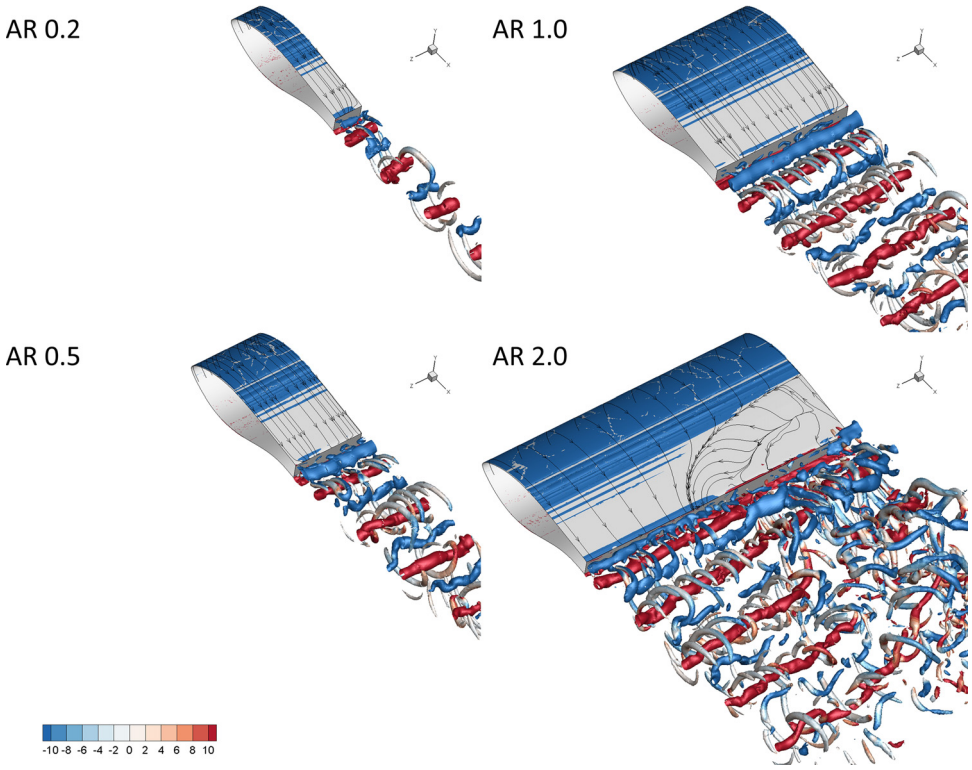

FIG. 9. Q criterion instantaneous isosurfaces of Q = 100 colored by spanwise vorticity and instantaneous surface flow lines. IDDES simulations of different aspect ratio values at $\alpha = 14°$ and $Re = 1.5 \times 10^6$. The surface flow lines for $AR = 2.0$ indicate stall cell formation.

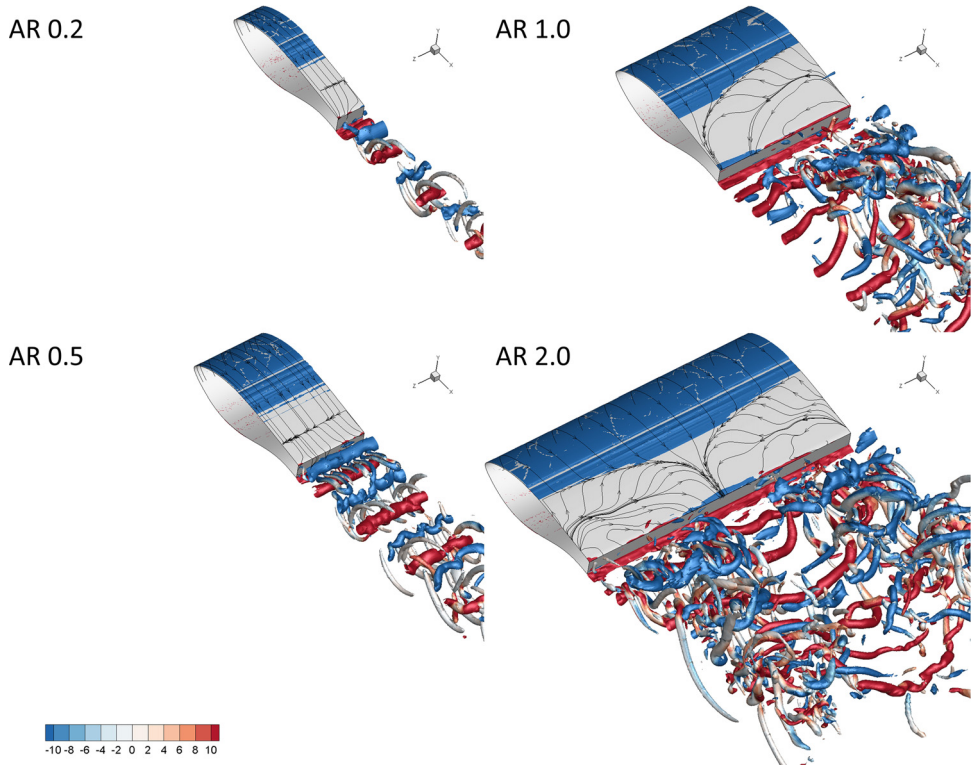

FIG. 10. Q criterion instantaneous isosurfaces of Q = 100 colored by spanwise vorticity and instantaneous surface flow lines. IDDES simulations of different aspect ratio values at $\alpha = 15^\circ$ and $\mathrm{Re} = 1.5 \times 10^6$. The surface flow lines for $AR = 1.0$ and $AR = 2.0$ indicate stall cell formation.

simulations. In the experiments, the low-drag range is $7.5^\circ < \alpha < 13.5^\circ$, see Fig. 6, right, practically equal to the range predicted by IDDES. For both IDDES and URANS predictions, this low-drag/drag variation pocket coincides with the reduced lift gradient range, which indicates a more generic change in the flow structure.

The correlation between the IDDES lift and drag coefficient signals is given in Fig. 12, left. It is observed that the correlation increases as the AoA increases until $\alpha = 14^\circ$, where there is a sudden drop. In the low-drag range ($7^\circ \leq \alpha \leq 13^\circ$), the two signals are strongly correlated ($r_{cor} > 0.9$).

The results (mean force coefficient gradient, standard deviation and correlation) suggest that the prestall regime can be split into two characteristically different regimes, namely, the low AoA and what is named here as the low-drag pocket regime.

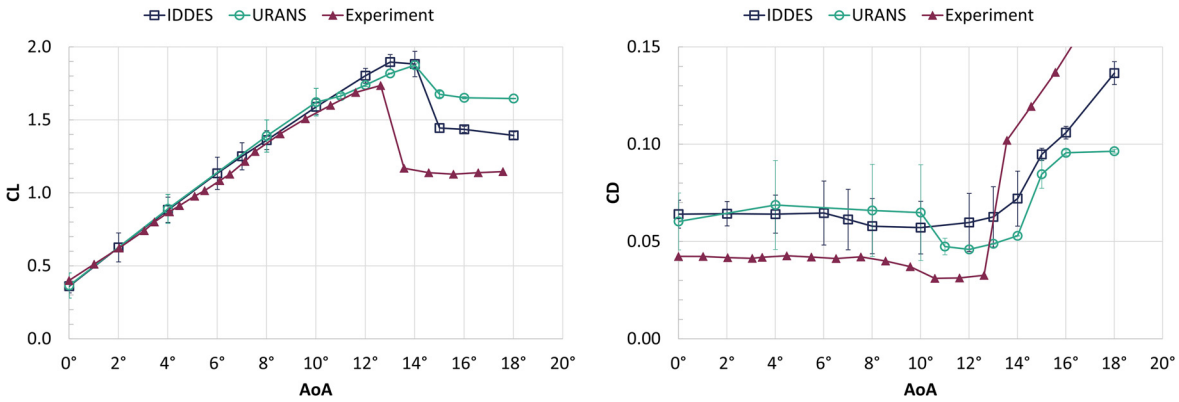

FIG. 11. Lift (left) and drag (right) coefficient variation with angle of attack for the IDDES and the URANS simulations, AR = 1.0 and $\mathrm{Re} = 1.5 \times 10^6$. The error bars show standard deviation of the relative quantity. Experimental data from Ref. 5.

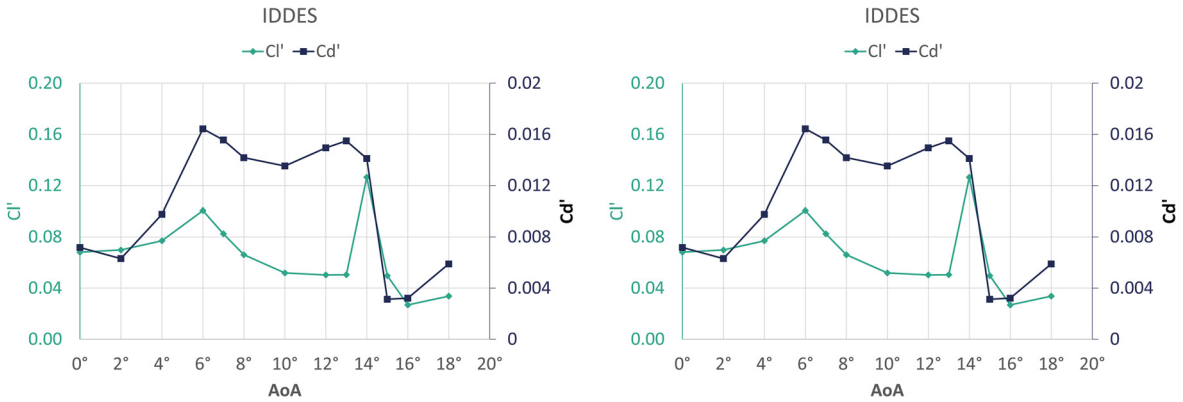

FIG. 12. Left: Lift and drag coefficient standard deviation variation with AoA. Right: Pearson correlation coefficient (r_{cor}) for the wing lift and drag coefficient signals. IDDES simulations, AR = 1.0 and Re = 1.5×10^6.

Frequency domain. The frequency content of the force coefficient time series at the selected AoA ($\alpha = 0$, $\alpha = 12$, and $\alpha = 16$) is shown in Fig. 13. The three AoA values were selected as representatives of the three identified flow regimes, namely, low AoA, low-drag pocket, post-stall. The Strouhal number is calculated based on the TE height ($St = \frac{fh_{TE}}{U_\infty}$). Lift and drag spectra have a peak at $St \approx 0.21$ at $\alpha = 0^\circ$ and $\alpha = 12^\circ$, which corresponds to bluff body shedding downstream of the blunt TE.

Looking closer at the frequency spectra, it is observed that at $\alpha = 12^\circ$ (low-drag pocket), the frequency peak about $St \approx 0.21$ is more concentrated than in the case of $\alpha = 0^\circ$ (low AoA range), where more broadband peak appears. The drag spectra also show a secondary peak at the second harmonic. This secondary peak is not as pronounced in the lift spectra. In the poststall region ($\alpha = 16^\circ$), the dominant frequency is very low, at St = 0.005 and the bluff body shedding frequency peak is no longer observed.

The St variation with AoA is given in Fig. 14, for all AoA. Only data from the lift spectra are presented here, in the interest of brevity, and it is worth mentioning that the findings would not change if the drag spectra were used. It is found that the bluff body shedding frequency is dominant up to $\alpha = 14^\circ$, or the $\alpha_{C_l,\max}$. Beyond this angle, very low dominant St numbers are observed.

It is noted at this point that very low frequencies have been observed in 3D separated flow over airfoils and more specifically when stall cells appear.[59–62] This low frequency has been attributed to a wholesale expansion/contraction of the stall cells[61] and, when normalized with the projection of the airfoil chord ($St_{c,proj} = \frac{fc\sin(\alpha)}{U_\infty}$), corresponds to Strouhal number of $St_{c,proj} \sim O(10^{-2})$. This nondimensional quantity is also plotted in Fig. 14 and, indeed, values close to the SC-related frequency are observed.

Spanwise correlation. The Pearson correlation coefficient (r) of the drag time series with respect to the midsection (placed at $z/b = 0$) for the IDDES simulations is shown in Fig. 15, for $\alpha = 0^\circ$ (low AoA), $\alpha = 12^\circ$ (low-drag pocket), and $\alpha = 16^\circ$ (post-stall range). For completeness, the correlation coefficient of the lift, drag, and pressure time series for the IDDES simulations and for all AoA is given in the Appendix, in Fig. 21.

According to Fig. 15, the flow spanwise correlation differs in the three identified flow regimes. At $\alpha = 0^\circ$, the flow at the ends of the computational domain is not correlated with the flow at the center of the wing. On the contrary, at $\alpha = 12^\circ$ the flow becomes strongly correlated across the wing span. In the post-stall regime ($\alpha = 16^\circ$) there is strong negative correlation between the flow at the ends of the computational domain. This is conceivably due to the stall cell that forms on the wing surface, as discussed later.

Wake structure

Bluff body wake flows at sufficiently high Reynolds numbers are inherently three-dimensional, dominated by two types of coherent structures, namely the von Kármán–Bénard spanwise vortices and the streamwise vortices, known as rolls and ribs, respectively. Rolls, which are the primary flow instability, experience small and large scale secondary instabilities.[63] Ribs are referred to as the small-scale, while roll dislocations are large scale secondary instabilities.[63]

The structures identified in the wake of the wing at various AoA can help explain the observed differences between the flow regimes. Figure 16 shows instantaneous isosurfaces of the Q criterion, at the top, and instantaneous contours of spanwise vorticity, at the bottom, for $\alpha = 0^\circ$ (low AoA), $\alpha = 12^\circ$ (low-drag pocket), and $\alpha = 16^\circ$ (post-stall range).

At low AoA, the wake is dominated by the presence of the von Kármán–Bénard vortices shed from both edges of the blunt TE. These vortices are three-dimensional with dislocations and oblique shedding, as expected. They also give rise to significant streamwise ribs, which resemble the secondary instabilities described in Ref. 28 although in that case the bluff body Re number was much smaller. At $\alpha = 12^\circ$, the number of ribs per unit span is considerably reduced and the wake appears significantly more organized than at $\alpha = 0^\circ$. It is noted that despite the stark difference in the wake structures, the flow over the airfoil is two-dimensional and very similar between the two cases (see surface streamlines in Fig. 16). In the post-stall case ($\alpha = 16^\circ$), the surface streamlines reveal the trace of half a stall cell, while the wake structures are significantly more complex and three-dimensional.

The wake for the low AoA cases ($\alpha = 0^\circ$, $\alpha = 12^\circ$) is examined further in terms of the vortex formation length, L_f, and the

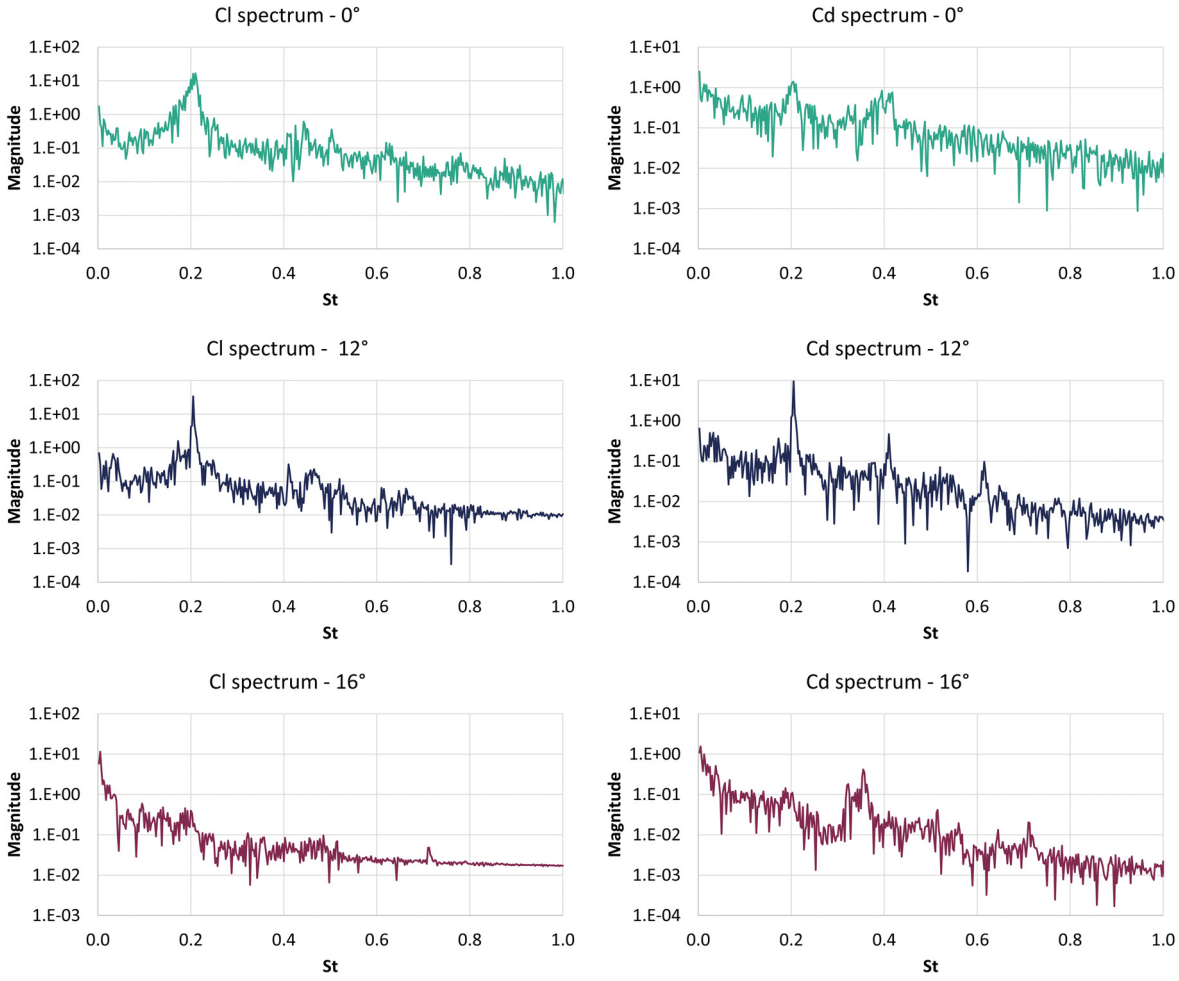

FIG. 13. Frequency spectrum based on the lift (left) and drag (right) coefficient time series for the IDDES simulations, AR = 1.0 and Re = 1.5×10^6. Top: $\alpha = 0°$, middle: $\alpha = 12°$, bottom: $\alpha = 16°$.

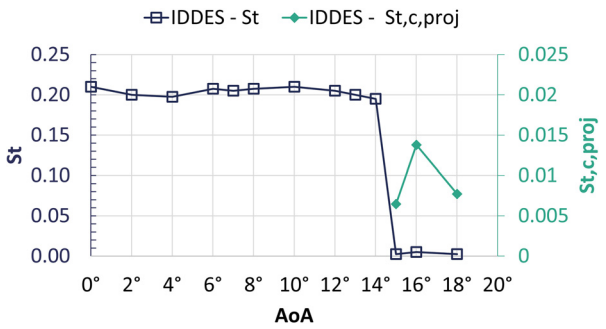

FIG. 14. Strouhal number based on the dominant frequency and trailing edge height ($St = \frac{fh_{TE}}{U_\infty}$) from the lift coefficient spectra for the IDDES simulations, AR = 1.0 and Re = 1.5×10^6. For the poststall angles of attack, the Strouhal number based on the projected chord length $\left[St_{c,proj} = \frac{fc\sin(\alpha)}{U_\infty}\right]$ is also given.

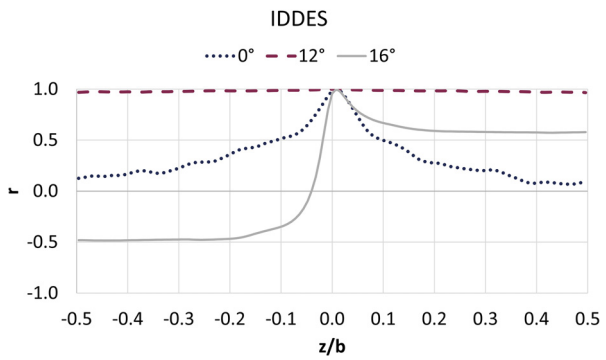

FIG. 15. Pearson correlation coefficient (r) of the drag coefficient time series with respect to the midsection (placed at $z/b = 0$) for IDDES simulations at various angles of attack and Re = 1.5×10^6.

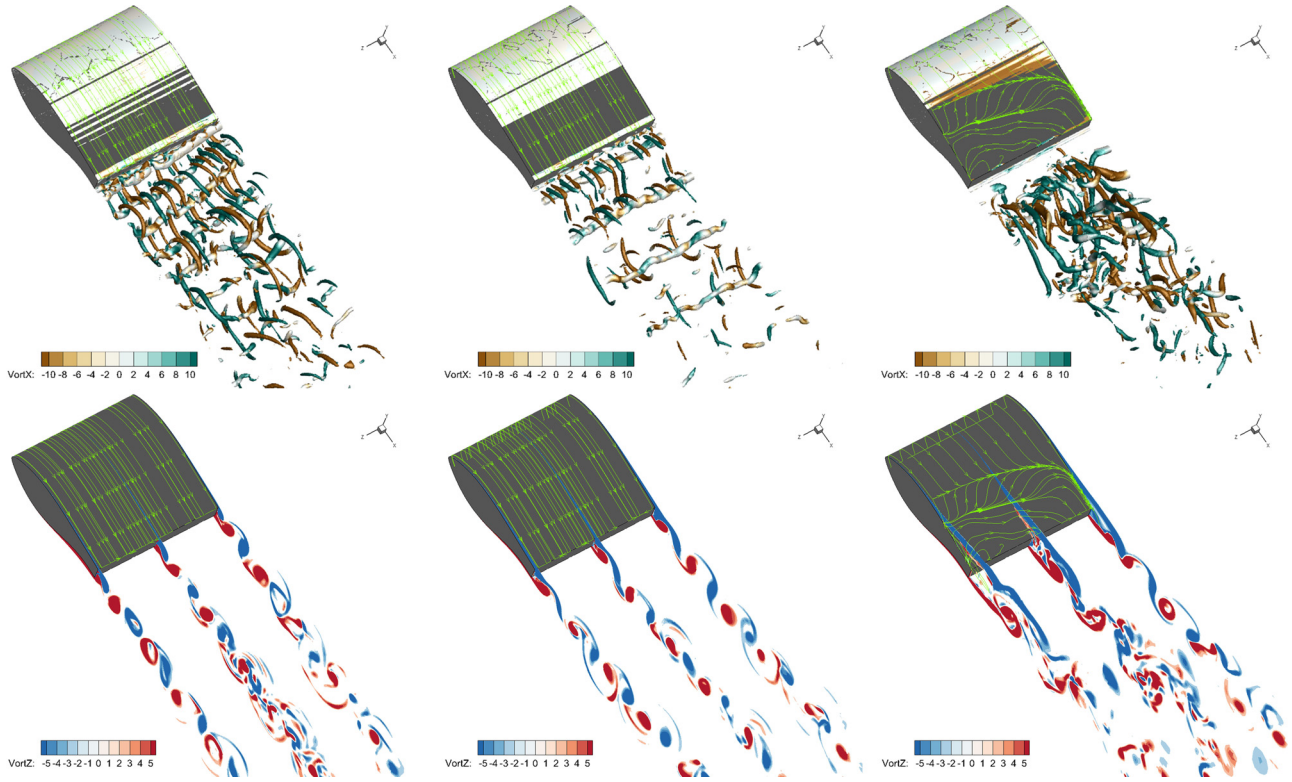

FIG. 16. (Top) Instantaneous isosurfaces of Q = 250, colored by streamwise vorticity (VortX) with surface streamlines for the IDDES simulations. (Bottom) Instantaneous contours of spanwise vorticity (VortZ) on three planes parallel to the flow at z/b = −0.5, z/b = 0 and z/b = 0.5, for AR = 1.0 and Re = 1.5×10^6. Left: $\alpha = 0°$, center: $\alpha = 12°$, right: $\alpha = 16°$. Contour levels from −2 to 2 are not shown for clarity.

wavelengths involved in the flow. The formation length is defined as the location of the maximum wake velocity fluctuation at the wake centerline[64] or, alternatively, as the position of the downstream edge of the recirculation zone along the wake centerline, determined based on the sectional streamlines of the mean flow field.[25] Here, for consistency with Refs. 25, 25, and 65, the latter definition is used and the values are given in Table I.

The prediction at 0°, $L_f \approx 0.75h_{TE}$, is in excellent agreement with the wind tunnel measurements[5] and in very good agreement with previous bluff body wake studies,[25,28,65] where $L_f \approx 0.82$. It is noted that the latter studies concerned flows with lower bluff body Reynolds numbers, $Re(d) \leq 50 \times 10^3$, where d is the bluff body thickness. In the present case, the Reynolds number based on the TE thickness is $Re_{TE} = \frac{\rho U h_{TE}}{\mu} = 159 \times 10^3$. Formation length is strongly correlated with base pressure and base drag in bluff body flows[5,66] and, indeed, the formation length increase at $\alpha = 12°$ corresponds to the observed profile drag decrease.

The spatial structure of the primary instability, the von Kármán–Bénard vortex street, is quantified by its wavelength, λ_x, defined as the streamwise distance between two consecutive vortices shed from the same edge of the blunt TE. Again, for consistency with previous studies, λ_x can be determined according to the equation $\lambda_x = \frac{U_c}{f_s}$, where f_s is the shedding frequency and U_c is the convective velocity. The latter is defined as the mean velocity on the wake centerline at a distance $4h_{TE}$ from the wing TE. In the present case, this is at $x = 1.424c$. The values are given in Table I and, again, the 0° value, $\lambda_x \approx 3.6h_{TE}$, is in very good agreement with the bluff body studies at lower Reynolds numbers,[25,28,65] where $\lambda_x \approx 3.7h_{TE}$. In the low-drag regime ($\alpha = 12°$), the primary instability wavelength is reduced to $\lambda_x \approx 3.3h_{TE}$.

The small-scale secondary instability (streamwise vortex ribs) is quantified by the spanwise wavelength, λ_z, which is a function of flow geometry, bluff body length to thickness ratio, Reynolds number, and inflow turbulence characteristics.[67–69] The interaction of ribs and rolls leads to velocity undulations of streamwise velocity on the XZ plane, which can be used to estimate the spanwise wavelength of the secondary instability.[68,70] Figures 17 and 18 show instantaneous Q criterion isosurfaces and the velocity undulations on a XZ plane at $y/c = 0.04$ for $\alpha = 0°$ and $\alpha = 12°$, respectively. The spanwise wavelength is found to be $\lambda_z \approx 1.0h_{TE}$ at $\alpha = 0°$ and $\lambda_z \approx 1.4h_{TE}$ at $\alpha = 12°$. The vortex structure is similar to the model proposed in Refs. 25 and 28, especially at $\alpha = 12°$. Instantaneous velocity data from Ref. 25 also suggest similar spanwise wavelength values ($\lambda_z \approx 1.25d$, from Figs. 8 and 14, in Ref. 25). It is noted that in Refs. 25 and 28, a POD based method was used to estimate the spanwise wavelength and the value $\lambda_z \approx 2.4d$ was found. Later, however, it was shown that the implemented analysis was inadequate and it was suggested that a more complete proper orthogonal decomposition analysis would lead to lower spanwise wavelength values, similar to the ones reported here.[71]

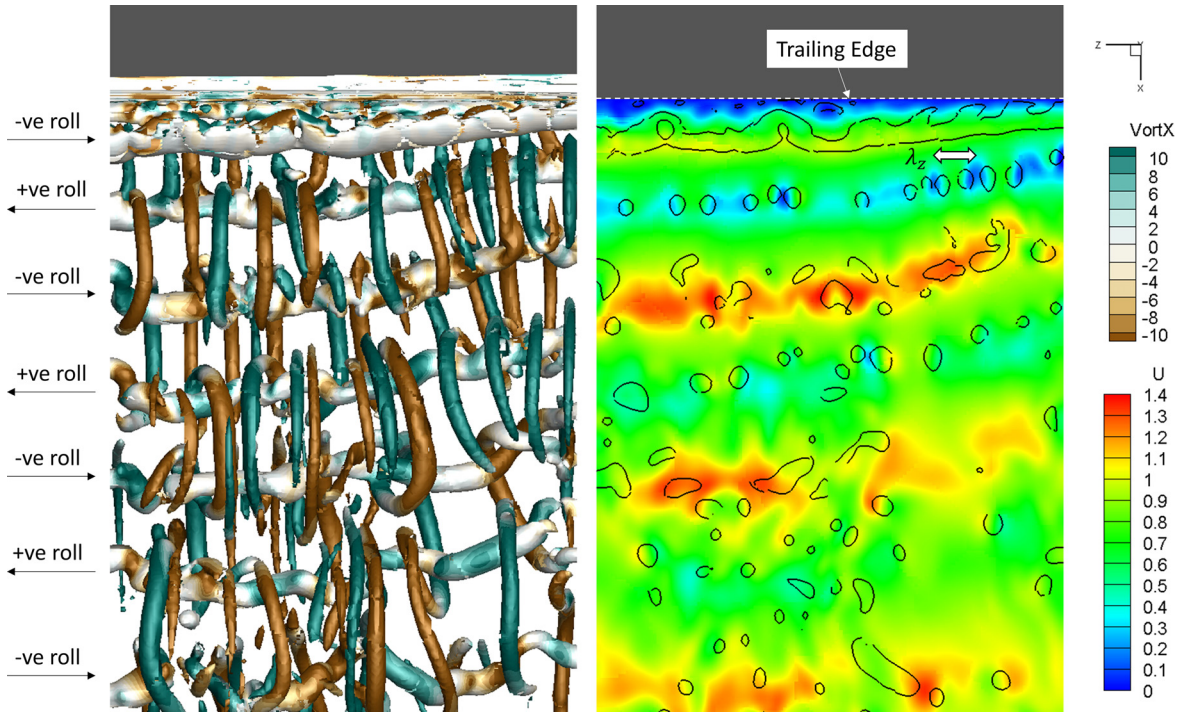

FIG. 17. IDDES simulations, $\alpha = 0°$, AR = 1.0 and Re = 1.5×10^6. (Left) Instantaneous isosurfaces of Q = 250, colored by streamwise vorticity (VortX). Contour levels from −2 to 2 are not shown for clarity. The vorticity direction of the streamwise rolls is indicated by the black vectors. (Right) Instantaneous contours of streamwise velocity (U) with Q isolines of Q = 250 on a XZ plane at y/c = 0.04. The spanwise wavelength of the secondary instability is also indicated.

In an experimental study of an airfoil with relatively thin finite trailing edge ($h_{TE} = 1.8\%$ chord),[26] it was found that the spanwise distribution of ribs does not change with incidence. However, that investigation was performed at significantly lower Reynolds numbers ($Re = 0.7 \times 10^6$, $Re_{TE} = 1.26 \times 10^4$) and the examined incidence range did not exceed $\alpha = 6°$. As discussed below, the increase in AoA at higher Re is an important factor, as the flow remains attached on the suction side of the airfoil, under conditions of increased adverse pressure gradient.

Figure 19 shows Q isosurfaces and spanwise vorticity contours for the time-averaged IDDES case at $\alpha = 0°$ (low AoA), $\alpha = 12°$ (low-drag pocket). The Q isosurface for the top vortex is much larger in the first case and, at the same time, the spanwise vorticity contours are much shorter, indicating a thinner boundary layer (BL) compared to the second case. At the same time, the lower vortex appears larger and stronger at $\alpha = 12°$, while the top vortex is significantly weaker and smaller. This happens because the BL on the suction side of the airfoil must overcome a significant adverse pressure gradient as the AoA increases. This decelerates the flow and the BL that feeds the vortex shed from the top edge of the TE (see also Refs. 10, 72, and 73).

These observations suggest that when we consider the unsteady vortex shedding from the wing TE, the vortices shed from the two edges are of comparable strength at $\alpha = 0°$, but this is not the case at $\alpha = 12°$, where the vortices shed from the lower edge will be much stronger. It is conceivable that this difference leads to different vortex interaction in the wake and, as a result, to the different wake structure in the low-drag pocket regime ($\alpha = 12°$) compared to the low AoA regime ($\alpha = 0°$).

The discussion of the complex vortex shedding behavior at high AoA is limited to qualitative terms, given the discrepancies between simulations and experiments highlighted in Fig. 6. Figure 20 shows where spanwise vorticity contours are plotted on three planes normal to the wing span. In this case, which is identical to the case shown in Fig. 10, top right, half a SC appears on the wing. The end of the SC is at the left-hand side of the wing while the center of the SC is at the right-hand side, where the separation line is at its most upstream location.

Looking at the vorticity contours in Fig. 20, we observe that the separation shear layer (blue in Fig. 20) is shed from different chordwise locations on the wing suction side, due to the presence of the SC and the three-dimensional separation line. The separation shear layer is hence markedly three-dimensional and so is its roll up into discreet vortices. The separation line is also not fixed and the most upstream separation location varies by 0.2c for the images shown in Fig. 20.

The lower edge shear layer (red in Fig. 20) on the other hand, has a fixed shedding point and is always shed from the lower edge of the blunt TE. As such it always leaves the wing in relatively two-dimensional form. The roll-up of the lower shear layer is affected by the three-dimensionality of the top shear layer.

At the left end of the wing, i.e., at the side of the stall cell, the shedding strongly resembles a von Kármán–Bénard vortex street. Both shear layers roll up into discrete spanwise vortices in a highly organized manner. At the other end of the wing, i.e., at the center of

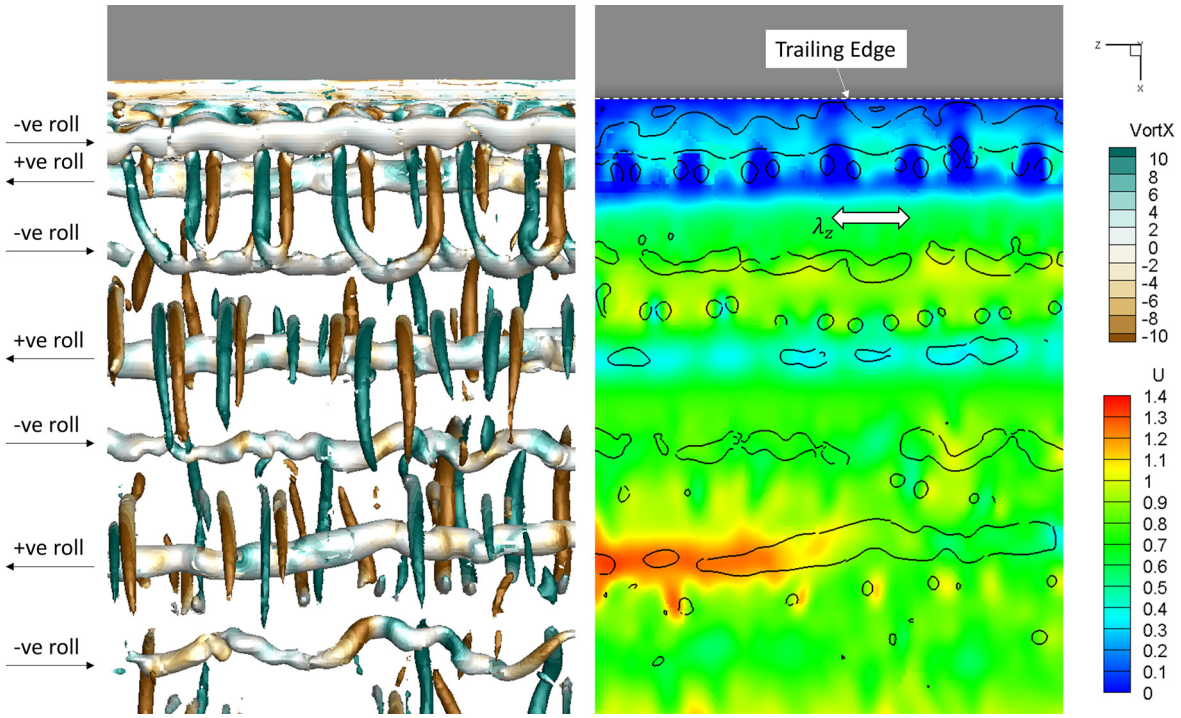

FIG. 18. IDDES simulations, $\alpha = 12°$, AR = 1.0 and $Re = 1.5 \times 10^6$. (Left) Instantaneous isosurfaces of Q = 250, colored by streamwise vorticity (VortX). Contour levels from −2 to 2 are not shown for clarity. The vorticity direction of the streamwise rolls is indicated by the black vectors. (Right) Instantaneous contours of streamwise velocity (U) with Q isolines of Q = 250 on a XZ plane at y/c = 0.04. The spanwise wavelength of the secondary instability is also indicated.

the stall cell, again both layers roll into discrete vortices, however, this happens in a less canonical way and the vortices are now larger. The lower right image in Fig. 20 also shows isosurfaces of the Q-criterion. The three-dimensional structures highlight the complexity of the flow and show how the spanwise vortices are affected by the presence of the stall cell.

DISCUSSION AND CONCLUSIONS

In the present study, the flow past a flatback wind turbine airfoil has been investigated for a range of AoA. Both IDDES and URANS simulations were performed and validated against experimental data. The flow phenomena involved in this case, such as bluff body vortex

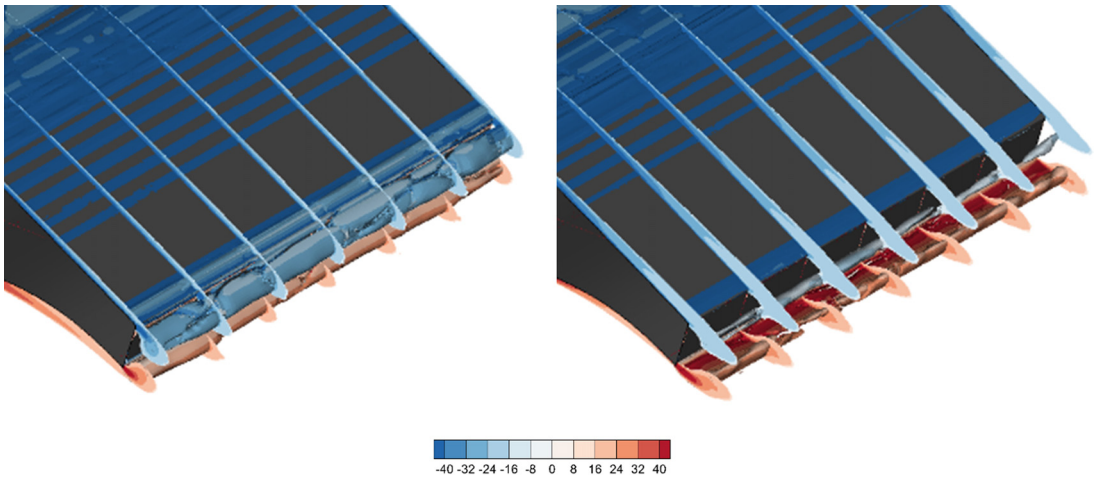

FIG. 19. Time-averaged isosurfaces of Q = 50, colored by spanwise vorticity with contours of spanwise vorticity on planes parallel to the flow at z/b = −0.5, z/b = −0.333, z/b = −0.167, z/b = 0, z/b = 0.167, z/b = 0.333 and z/b = 0.5, for the IDDES simulations with AR = 1.0 at $Re = 1.5 \times 10^6$. Left: $\alpha = 0°$, right: $\alpha = 12°$. Contour levels from −16 to 16 are not shown for clarity.

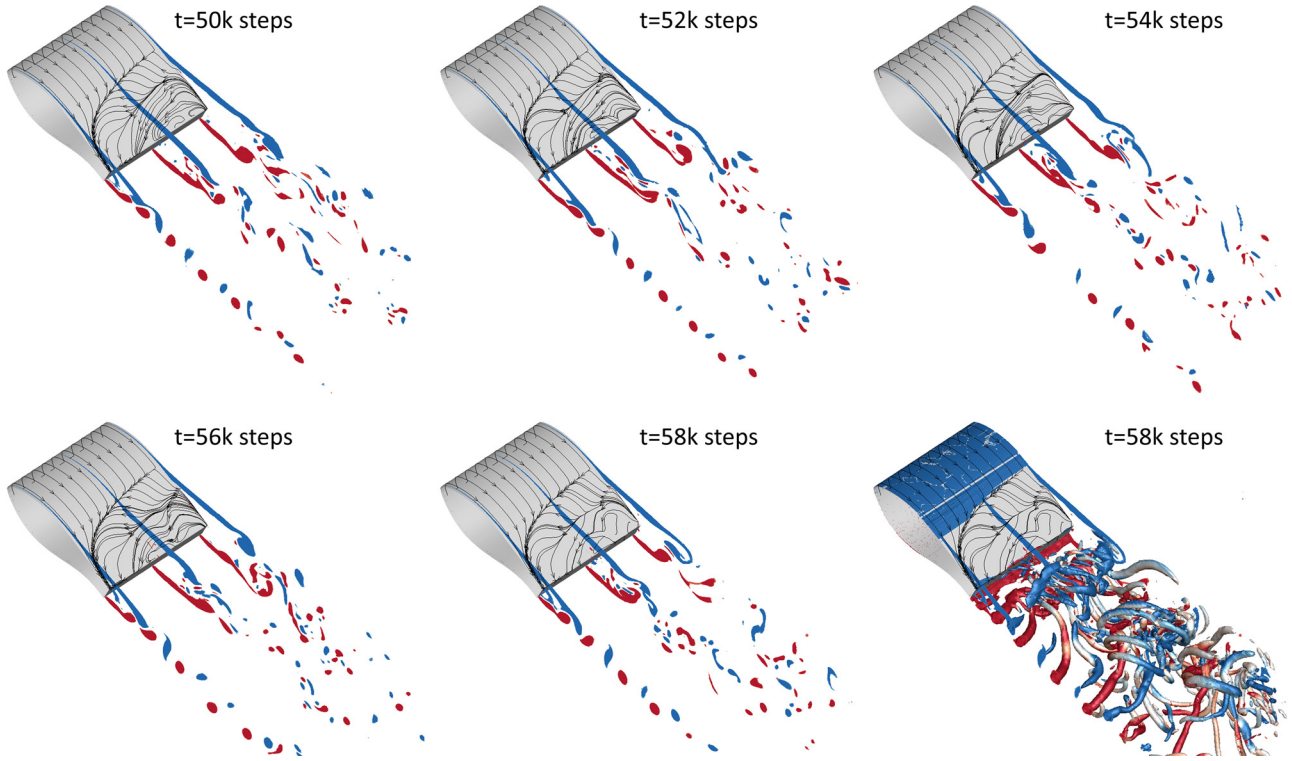

FIG. 20. Instantaneous contours of spanwise vorticity on three planes parallel to the flow at z/b = −0.5, z/b = 0 and z/b = 0.5, for AR = 1.0 and Re = 1.5×10^6, $\alpha = 15°$. Contour levels: red: −10 to −9 and blue: 9 to 10. The last two figures are the same, but on the lower right one, Q criterion instantaneous isosurfaces of Q = 100 colored by spanwise vorticity are also shown to highlight the complexity of the flow.

shedding and stall cell formation, are inherently unsteady and three-dimensional and a challenge for the CFD community.

Results show that the selection of CFD modeling approach (URANS or IDDES) is not as important as the spanwise extent of the computational domain. In fact, when applied on the same mesh of $AR = 1.0$, there is good agreement between IDDES and URANS predictions in (a) force coefficient values at low AoA (b) $\alpha_{C_l,\max}$ prediction and (c) the fact that a low-drag pocket regime is predicted in both cases.

On the other hand, the spanwise extent of the computational domain has been found to be crucial. More specifically, it is found that for both 3D phenomena involved in this flow (bluff body vortex shedding and stall cell formation) to develop unrestrained, the AR needs to be greater than 0.5. At lower angles of attack, AR values lower or equal to 0.5 artificially constrain the 3D character of the bluff body wake. Limiting the computational domain width to less than less than $5h_{TE}$ and enforcing symmetry conditions at the lateral boundaries significantly alters the vorticity evolution in the wake. Still, all simulations predict a dominant frequency of St $\approx$ 0.21, which suggests that even the lowest AR simulations are able to capture the dynamics of the primary instability (bluff body spanwise vortex shedding).

With regard to higher AoA flow, it is found that when the spanwise extent of the computational domain is limited ($AR \leq 0.5$), the formation of stall cells is prevented and, as a result, $\alpha_{C_l,\max}$ is overpredicted. Stall cells appear slightly earlier for $AR = 2.0$ than for $AR = 1.0$, but the $\alpha_{C_l,\max}$ remains the same for the two cases, practically equal to that of the experiments. The number of stall cells per unit span is the same for $AR = 1.0$ and $AR = 2.0$ simulations for $\alpha \geq 15°$.

The flow past the airfoil was further investigated based on the $AR = 1.0$ IDDES simulations. To the best of the authors' knowledge, a low-drag pocket regime at AoA just before $\alpha_{C_l,\max}$ has been identified and analyzed for the first time. This pocket is observed in the experiments, IDDES and URANS simulations. Previous studies did report lower drag values in the pre-stall region, but the phenomenon was not investigated further. The existence of a separate, low-drag regime is confirmed by lift and drag coefficient mean values and signal behavior along with wake structures, frequency content, and spanwise correlations. Furthermore, the vortex formation length and the wavelength of the secondary instability increase, while the wavelength of the primary instability decreases. Conceivably, this structure change is linked to the reduction and increase in strength of the top and lower vortex, respectively, in the bluff body wake. The vortices are no longer comparable in strength and their interaction in the wake is no longer as strong and three-dimensional as it was at low AoA.

At AoA beyond $\alpha_{C_l,\max}$, the wake is highly complex and three-dimensional. Both shear layers, the separation and lower edge, roll-up in discreet vortices. The roll-up is more structured at the side of the SC. On the other hand, at the center of the SC, the roll-up is more complex and less canonical. The presence of the stall cells leads to bent and highly 3D vortical structures.

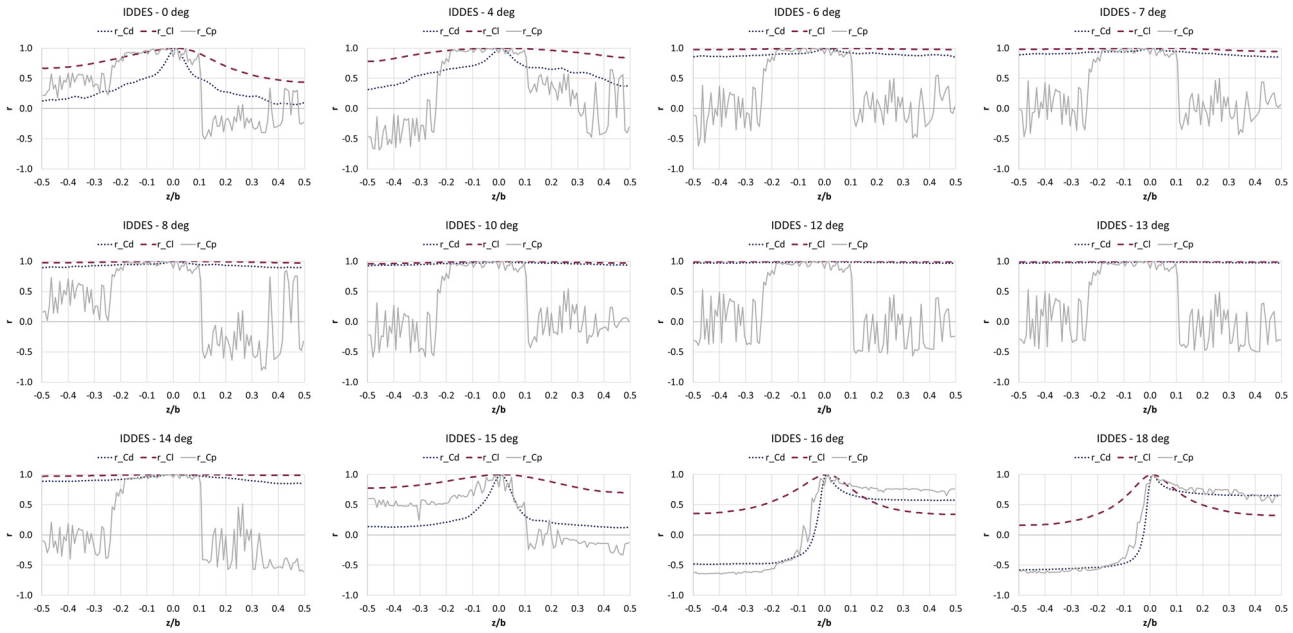

FIG. 21. Pearson correlation coefficient (r) of the lift (r_Cl), drag (r_Cd) and pressure (r_Cp) time series with respect to the midsection (placed at z/b = 0) for IDDES simulations of aspect ratio AR = 1.0, at Re = 1.5×10^6 and various angles of attack. The pressure correlation is with respect to the pressure at a point located on the TE, at mid-height and at midspan [i.e., at (x/c, y/c, z/b) = (1, 0, 0)]. Highly positive values indicate strong positive correlation, and highly negative values suggest a strong negative correlation.

ACKNOWLEDGMENTS

Computational resources were provided by HPC Wales, which is gratefully acknowledged.

M. Manolesos would like to acknowledge the contribution of the Supergen Early Career Researcher Fund Award from the Supergen Offshore Renewable Energy Hub, EPSRC.

APPENDIX: SPANWISE PEARSON CORRELATION COEFFICIENT

Pearson correlation coefficient (r) of the lift (r_Cl), drag (r_Cd), and pressure (r_Cp) time series with respect to the midsection (placed at z/b = 0) for IDDES simulations of aspect ratio AR = 1.0, at Re = 1.5×10^6 and various angles of attack.

DATA AVAILABILITY

The data that support the findings of this study are available from the corresponding author upon reasonable request.

REFERENCES

[1]D. T. Griffith and P. W. Richards, "The SNL100-03 blade: Design studies with flatback airfoils for the sandia 100-meter blade," Technical Report No. SAND2014-18129 (Sandia National Laboratory, 2014).
[2]C. Noyes, E. Loth, D. Martin, K. Johnson, G. Ananda, and M. Selig, "Extreme-scale load-aligning rotor: To hinge or not to hinge?," Appl. Energy **257**, 113985 (2020).
[3]J. P. Baker, E. A. Mayda, and C. P. Van Dam, "Experimental analysis of thick blunt trailing-edge wind turbine airfoils," J. Sol. Energy Eng. **128**, 422–431 (2006).
[4]M. Manolesos, G. Papadakis, and S. Voutsinas, "Study of drag reduction devices on a flatback airfoil," AIAA Paper No. 2016-0517, 2016.
[5]M. Manolesos and S. G. Voutsinas, "Experimental study of drag-reduction devices on a flatback airfoil," AIAA J. **54**, 3382–3396 (2016).
[6]M. F. Barone and D. Berg, "Aerodynamic and aeroacoustic properties of a flatback airfoil: An update," AIAA Paper No. 2009-271, 2009.
[7]M. Doosttalab and O. Frommann, "Multidisciplinary design and verification of the HB flatback airfoil family," AIAA J. **57**, 4639–4649 (2019).
[8]C. Stone, M. Barone, M. Smith, and E. Lynch, "A computational study of the aerodynamics and aeroacoustics of a flatback airfoil using hybrid RANS-LES," AIAA Paper No. 2009-273, 2009.
[9]L. Hongpeng, W. Yu, Y. Rujing, X. Peng, and W. Qing, "Influence of the modification of asymmetric trailing-edge thickness on the aerodynamic performance of a wind turbine airfoil," Renewable Energy **147**, 1623–1631 (2020).
[10]G. Papadakis and M. Manolesos, "The flow past a flatback airfoil with flow control devices: Benchmarking numerical simulations against wind tunnel data," Wind Energy Sci. **5**, 911–927 (2020).
[11]G. Papadakis, M. Manolesos, K. Diakakis, and V. A. Riziotis, "DES vs RANS: The flatback airfoil case," J. Phys.: Conf. Ser. **1618**, 052062 (2020).
[12]G. Papadakis and S. G. Voutsinas, "A strongly coupled Eulerian Lagrangian method verified in 2D external compressible flows," Comput. Fluids **195**, 104325 (2019).
[13]J. P. Baker and C. P. van Dam, "Drag reduction of blunt trailing-edge airfoils," in Proceedings of the International Colloquium on Bluff Bodies Aerodynamics and Applications, Milan, Italy, 20–24 July 2008, http://bbaa6.mecc.polimi.it/uploads/validati/TBAF03.pdf
[14]G. Wang, L. Zhang, and W. Z. Shen, "LES simulation and experimental validation of the unsteady aerodynamics of blunt wind turbine airfoils," Energy **158**, 911–923 (2018).
[15]M. Manolesos, G. Papadakis, and S. Voutsinas, "An experimental and numerical investigation on the formation of stall-cells on airfoils," J. Phys.: Conf. Ser. **555**, 012068 (2014).
[16]M. Manolesos and S. G. Voutsinas, "Study of a stall cell using stereo particle image velocimetry," Phys. Fluids **26**, 045101 (2014).
[17]M. Manolesos, G. Papadakis, and S. G. Voutsinas, "Experimental and computational analysis of stall cells on rectangular wings," Wind Energy **17**, 939–955 (2014).

[18]K. Zhang, S. Hayostek, M. Amitay, W. He, V. Theofilis, and K. Taira, "On the formation of three-dimensional separated flows over wings under tip effects," J. Fluid Mech. **895**, A9 (2020).
[19]E. P. DeMauro, H. Dell'Orso, V. Sivaneri, B. A. Tuna, and M. Amitay, "Measurements of 3-D stall cells on 2-D airfoils," AIAA Paper No. 2015-2633, 2015.
[20]A. P. Broeren and M. B. Bragg, "Spanwise variation in the unsteady stalling flowfields of two-dimensional airfoil models," AIAA J. **39**, 1641–1651 (2001).
[21]H. A. Smith and R. F. Schaefer, "Aerodynamic characteristics at Reynolds numbers of 3.0 × 10 (6) and 6.0 × 10 (6) of three airfoil sections formed by cutting off various amounts from the rear portion of the NACA 0012 airfoil section," Technical Report No. TN-2074 (NACA, 1950).
[22]M. L. Post, R. B. Jones, A. W. Denton, and R. Millard, "Characterization of a flatback airfoil for use in wind power generation," AIAA Paper No. 2008-1330, 2008, pp. 1330–2008.
[23]T. Winnemöller and C. P. Van Dam, "Design and numerical optimization of thick airfoils including blunt trailing edges," J. Aircr. **44**, 232–240 (2007).
[24]N. N. Sørensen, "A small study of flatback airfoils," in *Proceedings of the Aeroelastic Work—Latest Results from AeroOpt* (Danmarks Tekniske Universitet, Risø Nationallaboratoriet for Bæredygtig Energi, 2011), pp. 153–195, see www.risoe.dtu.dk; accessed 27 April 2021.
[25]A. Naghib-Lahouti, P. Lavoie, and H. Hangan, "Wake instabilities of a blunt trailing edge profiled body at intermediate Reynolds numbers," Exp. Fluids **55**, 1–15 (2014).
[26]M. El-Gammal and H. Hangan, "Three-dimensional wake dynamics of a blunt and divergent trailing edge airfoil," Exp. Fluids **44**, 705–717 (2008).
[27]R. M. Darekar and S. J. Sherwin, "Flow past a square-section cylinder with a wavy stagnation face," J. Fluid Mech. **426**, 263–295 (2001).
[28]A. Naghib-Lahouti, L. S. Doddipatla, and H. Hangan, "Secondary wake instabilities of a blunt trailing edge profiled body as a basis for flow control," Exp. Fluids **52**, 1547–1566 (2012).
[29]S. J. Yang and J. D. Baeder, "Blunt-wavy combined trailing edge for wind turbine blade inboard performance improvement," J. Phys.: Conf. Ser. **1037**, 022004 (2018).
[30]A. Naghib-Lahouti, H. Hangan, and P. Lavoie, "Distributed forcing flow control in the wake of a blunt trailing edge profiled body using plasma actuators," Phys. Fluids **27**, 035110 (2015).
[31]C. Stone, S. Tebo, and E. P. N. Duque, "Computational fluid dynamics of flatback airfoils for wind turbine applications," AIAA Paper No. 2006-194, 2006.
[32]G. Papadakis, K. Diakakis, and M. Manolesos, "A detached eddy simulation study of drag reduction devices for flatback airfoils," in *Proceedings of the Wind Energy Science Conference* (EAWE, Cork, Ireland, 2019).
[33]J. Calafell, O. Lehmkuhl, I. Rodriguez, and A. Oliva, "On the large-eddy simulation modelling of wind turbine dedicated airfoils at high Reynolds numbers," in *Proceedings of the Seventh International Symposium on Turbulence Heat and Mass Transfer* (ICHMT Digital Library Online, 2012), pp. 1419–1430.
[34]O. Lehmkuhl, J. Calafell, I. Rodríguez, and A. Oliva, "Large-eddy simulations of wind turbine dedicated airfoils at high Reynolds numbers," in *Wind Energy-Impact of Turbulence*, edited by M. Hölling, J. Peinke, and S. Ivanell (Springer, Berlin, Heidelberg, 2014), pp. 147–152.
[35]K. J. Standish and C. P. van Dam, "Aerodynamic analysis of blunt trailing edge airfoils," J. Sol. Energy Eng. **125**, 479–487 (2003).
[36]T. Kim, M. Jeon, S. Lee, and H. Shin, "Numerical simulation of flatback airfoil aerodynamic noise," Renewable Energy **65**, 192–201 (2014).
[37]H. Xu, W. Shen, W. Zhu, H. Yang, and C. Liu, "Aerodynamic analysis of trailing edge enlarged wind turbine airfoils," J. Phys.: Conf. Ser. **524**, 012010 (2014).
[38]N. Thomareis and G. Papadakis, "Effect of trailing edge shape on the separated flow characteristics around an airfoil at low Reynolds number: A numerical study," Phys. Fluids **29**, 014101 (2017).
[39]T. A. Smith and Y. Ventikos, "Boundary layer transition over a foil using direct numerical simulation and large eddy simulation," Phys. Fluids **31**, 124102 (2019).
[40]K. Taira and T. Colonius, "Three-dimensional flows around low-aspect-ratio flat-plate wings at low Reynolds numbers," J. Fluid Mech. **623**, 187–207 (2009).
[41]M. Manolesos, "Experimental and computational study of three-dimensional separation and separation control using passive vortex generators," Ph.D. thesis (NTUA, 2013), see http://www.aerolab.mech.ntua.gr/ManolesosPhD.pdf
[42]F. Bertagnolio, N. N. Sørensen, and J. Johansen, "Profile catalogue for airfoil sections based on 3D computations," Technical Report No. RISO-R-1581(EN) (RISØ National Laboratory, Roskilde, 2006).
[43]D. Ntouras and G. Papadakis, "A coupled artificial compressibility method for free surface flows," J. Mar. Sci. Eng. **8**, 590 (2020).
[44]P. L. Roe, "Approximate Riemann solvers, parameter vectors, and difference schemes," J. Comput. Phys. **43**, 357–372 (1981).
[45]V. Venkatakrishnan, "On the accuracy of limiters and convergence to steady state solutions," AIAA Paper No. 93-0881, 1993.
[46]R. T. Biedron, V. N. Vatsa, and H. L. Atkins, "Simulation of unsteady flows using an unstructured Navier-Stokes solver on moving and stationary grids," AIAA Paper No. 2005-5093, 2005, pp. 1167–1183.
[47]P. Spalart and S. Allmaras, "A one-equation turbulence model for aerodynamic flows," AIAA Paper No. 92-0440, 1992, pp. 5–21.
[48]F. R. Menter, "Two-equation eddy-viscosity turbulence models for engineering applications," AIAA J. **32**, 1598–1605 (1994).
[49]M. L. Shur, P. R. Spalart, M. K. Strelets, and A. K. Travin, "A hybrid RANS-LES approach with delayed-DES and wall-modelled LES capabilities," Int. J. Heat Fluid Flow **29**, 1638–1649 (2008).
[50]N. N. Sørensen, A. S. Olsen, C. Bak, M. Gaunaa, J. S. Beckerlee, A. Fischer, R. F. Mikkelsen, and S. Ildvedsen, "CFD modeling of the Poul la Cour tunnel," J. Phys.: Conf. Ser. **1618**, 052047 (2020).
[51]N. N. Sørensen, B. Méndez, A. Muñoz, G. Sieros, E. Jost, T. Lutz, G. Papadakis, S. Voutsinas, G. N. Barakos, S. Colonia, D. Baldacchino, C. Baptista, and C. Ferreira, "CFD code comparison for 2D airfoil flows," J. Phys.: Conf. Ser. **753**, 082019 (2016).
[52]D. S. Kamenetskiy, J. E. Bussoletti, C. L. Hilmes, V. Venkatakrishnan, L. B. Wigton, and F. T. Johnson, "Numerical evidence of multiple solutions for the Reynolds-averaged Navier–Stokes equations," AIAA J. **52**, 1686–1698 (2014).
[53]K. Boorsma, A. Muñoz, B. Méndez, S. Gómez, A. Irisarri, X. Munduate, G. Sieros, P. Chaviaropoulos, S. G. Voutsinas, J. Prospathopoulos, M. Manolesos, W. Z. Shen, W. Zhu, H. Madsen, Sieros, P. Chaviaropoulos, S. G. Voutsinas, J. Prospathopoulos, M. Manolesos, W. Z. Shen, W. Zhu, and H. Madsen, "New airfoils for high rotational speed wind turbines," INNWIND. EU Deliverable Report No. 2.12, 2015.
[54]J. C. R. Hunt, A. A. Wray, and P. Moin, "Eddies, streams, and convergence zones in turbulent flows," in *Proceedings of the 1988 Summer Program of the Center for Turbulence Research* (NASA Ames/Stanford University, 1988), Vol. 2, pp. 193–208.
[55]V. Kolář, "Vortex identification: New requirements and limitations," Int. J. Heat Fluid Flow **28**, 638–652 (2007).
[56]A. E. Winkelmann, "An experimental study of mushroom shaped stall cells," AIAA Paper No. 82-0942, 1982.
[57]M. Manolesos and S. G. Voutsinas, "Experimental investigation of the flow past passive vortex generators on an airfoil experiencing three-dimensional separation," J. Wind Eng. Ind. Aerodyn. **142**, 130–148 (2015).
[58]D. Baldacchino, C. Ferreira, D. De Tavernier, W. A. Timmer, and G. J. W. van Bussel, "Experimental parameter study for passive vortex generators on a 30% thick airfoil," Wind Energy **21**, 745–765 (2018).
[59]S. A. Yon and J. Katz, "Study of the unsteady flow features on a stalled wing," AIAA J. **36**, 305–312 (1998).
[60]K. J. Disotell and J. W. Gregory, "Time-resolved measurements of cellular separation on a stalling airfoil," AIAA Paper No. 2015-1501, 2015.
[61]M. G. C. Garland, M. S. Santer, and J. F. Morrison, "Control of cellular separation using adaptive surfaces," J. Fluids Struct. **91**, 102609 (2019).
[62]M. A. Khan, "Dynamic stall modeling for wind turbines," Master's thesis (TU Delft, 2018), see http://repository.tudelft.nl/; accessed 28 May 2020.
[63]C. H. K. K. Williamson, "Vortex dynamics in the cylinder wake," Annu. Rev. Fluid Mech. **28**, 477–539 (1996).
[64]O. M. Griffin, "A note on bluff body vortex formation," J. Fluid Mech. **284**, 217–224 (1995).
[65]L. S. Doddipatla, H. Hangan, V. Durgesh, and J. Naughton, "Wake dynamics resulting from trailing-edge spanwise sinusoidal perturbation," AIAA J. **55**, 1833–1851 (2017).
[66]P. W. Bearman, "Investigation of the flow behind a two-dimensional model with a blunt trailing edge and fitted with splitter plates," J. Fluid Mech. **21**, 241–255 (1965).

[67]K. Ryan, M. C. Thompson, and K. Hourigan, "Three-dimensional transition in the wake of bluff elongated cylinders," J. Fluid Mech. **538**, 1 (2005).
[68]J. Wu, J. Sheridan, M. C. Welsh, and K. Hourigan, "Three-dimensional vortex structures in a cylinder wake," J. Fluid Mech. **312**, 201 (1996).
[69]G. J. Sheard, M. J. Fitzgerald, and K. Ryan, "Cylinders with square cross-section: Wake instabilities with incidence angle variation," J. Fluid Mech. **630**, 43 (2009).
[70]H. Mansy, P. M. Yang, and D. R. Williams, "Quantitative measurements of three-dimensional structures in the wake of a circular cylinder," J. Fluid Mech. **270**, 277 (1994).
[71]B. Gibeau, C. R. Koch, and S. Ghaemi, "Secondary instabilities in the wake of an elongated two-dimensional body with a blunt trailing edge," J. Fluid Mech. **846**, 578–604 (2018).
[72]G. Papadakis and M. Manolesos (2020). "The flow past a flatback airfoil with flow control devices: Benchmarking numerical simulations against wind tunnel data—Animations II," Zenodo. (2020). https://doi:10.5281/ZENODO.3876198
[73]G. Papadakis and M. Manolesos (2020). "The flow past a flatback airfoil with flow control devices: Benchmarking numerical simulations against wind tunnel data—Animations," Zenodo. https://doi:10.5281/ZENODO.3662124